

Temporal Airy pulses for controlled high aspect ratio nanomachining of dielectrics

NADINE GÖTTE,¹ THOMAS WINKLER,¹ TAMARA MEINL,² THOMAS KUSSEROW,² BASTIAN ZIELINSKI,¹ CRISTIAN SARPE,¹ ARNE SENFTLEBEN,¹ HARTMUT HILLMER,² AND THOMAS BAUMERT^{1,*}

¹University of Kassel, Institute of Physics and CINSaT, Heinrich-Plett-Str. 40, 34132 Kassel, Germany

²University of Kassel, Institute of Nanostructure Technologies and Analytics and CINSaT, Heinrich-Plett-Str. 40, 34132 Kassel, Germany

*Corresponding author: baumert@physik.uni-kassel.de

Received 22 December 2015; revised 12 February 2016; accepted 25 February 2016 (Doc. ID 256290); published 5 April 2016

Understanding the interplay between optical pulse parameters and ultrafast material response is critical in achieving efficient and controlled laser nanomachining. In general, the key to initiate material processing is the deposition of a sufficient energy density within the electronic system. In dielectrics this critical energy density corresponds typically to a plasma frequency in the near-IR spectral region. Creating this density instantaneously with ultrashort laser pulses of a few tens of femtoseconds pulse duration in the same spectral region, the penetration depth into the material will strongly decrease with increasing electron density. Consequently, staying below this critical density will allow deep penetration depths. This calls for delayed ionization processes to deposit the energy for processing, thus introducing the temporal structure of the laser pulses as a control parameter. In this contribution we demonstrate this concept experimentally and substantiate the physical picture with numerical calculations. Bandwidth-limited pulses of 30 fs pulse duration are stretched up to 1.5 ps either temporally symmetrically or temporally asymmetrically. The interplay between pulse structure and material response is optimally exploited by the asymmetrically structured temporal Airy pulses leading to the inherently efficient creation of high aspect ratio nanochannels. Depths in the range of several micrometers and diameters around 250 nm are created within a single laser shot and without making use of self-focusing and filamentation processes. In addition to the machining of nanophotonic devices in dielectrics, the technique has the potential to enhance laser-based nanocell surgery and cell poration techniques. © 2016 Optical Society of America

OCIS codes: (220.4241) Nanostructure fabrication; (350.3390) Laser materials processing; (320.5540) Pulse shaping; (190.4180) Multiphoton processes.

<http://dx.doi.org/10.1364/OPTICA.3.000389>

1. INTRODUCTION

Dielectric materials are transparent from the IR over the visible into the UV spectral region and are therefore ideally suited for nanophotonic devices in the very same spectral range. Thus, machining methods in the few hundred nanometer range and below are necessary. However, the structuring of nonconductive dielectric materials by conventional processing techniques like electron beam lithography or focused ion beam (FIB) milling [1] suffers from the charging of the material's surface [2]. The implementation of ultrashort laser pulses as a direct patterning method is an attractive alternative, as this can overcome charging effects and also provide very fast processing times. Based on the high non-linearity of the laser-material interaction, the enhanced energy confinement, and limited heat diffusion, ultrashort laser pulses have become the instrument of choice for dielectric structuring on a micrometer or even nanometer scale [3] as well as for applications in nanosurgery [4,5].

Primary processes induced by ultrafast laser pulses involve nonlinear electronic excitation on the femtosecond time scale

and energy transfer to the lattice on the picosecond time scale, followed by phase transitions like ablation or melting. Thus, temporal laser control can facilitate synchronization between the light and the material response and therefore lead to an efficient coupling of the laser energy [6,7]. When restricting the excitation window to the femtosecond regime in order to confine heat diffusion, the generation of a sufficient energy density within the electronic system is the key parameter to initiate the abovementioned phase transitions. The transient free carrier density plays a fundamental role in determining the optical properties in addition to various propagation and relaxation mechanisms. Depending on intensity, free carriers are initially promoted into the conduction band by strong field excitation, i.e., multiphoton ionization (MPI) or tunnel ionization. These free electrons can further absorb energy by inverse bremsstrahlung and subsequently induce carrier multiplication by collisions. This process is often termed avalanche ionization (AI). A detailed overview of laser excitation in dielectrics can be found in Balling and Schou [8] and references therein. Optical damage thresholds were used as experimental

evidence for exceeding a certain critical electron density after the laser interaction, and the regulatory effect of pulse duration has been investigated over the last two decades [9,10]. Studies of transient electron densities range from intensities below [11,12] up to well above the breakdown threshold [13–15], confirming the described scenario. Optical damage thresholds were also used to demonstrate control of MPI and AI [16]. Furthermore, it has been demonstrated that direct structuring of dielectric materials with temporal Airy pulses (TAPs) generates reproducible surface structures reaching the sub-100-nm regime [17], which is an order of magnitude below the diffraction limit. Here, a first experimental indication was given that TAPs can create deeper structures as compared to bandwidth-limited pulses. Other approaches to creating high aspect ratio channels in dielectrics basically utilize spatial beam propagation based on self-focusing effects or Bessel beam generation and will be discussed later.

In this contribution we demonstrate the creation of high aspect ratio channels in fused silica by specifically temporally tailored femtosecond laser pulses in a power regime where self-focusing effects can be neglected. The findings are supported by rate equation simulations.

2. IDENTIFICATION OF THE TECHNOLOGICAL REQUIREMENTS

The physical picture behind our temporal pulse tailoring is quite intuitive: ablation of dielectrics is often attributed to a critical electron density of a pure electron-hole plasma in the range of 10^{21} electrons/cm³ rather than a critical energy density W within the electronic system. In the Drude model, the corresponding plasma frequency $\omega_{\text{pl}} = \sqrt{e^2 N_{\text{CB}} / m_e \epsilon_0}$ is in the near-IR, and laser light at 785 nm will start to be strongly absorbed, i.e., the penetration depth into the material will strongly decrease with increasing electron density. A special feature regarding the conduction band electron dynamics in fused silica is a fast mechanism leading to a rapid reduction of the electrons into a self-trapped exciton (STE) state, settled on a time scale of 150 fs [11]. The decrease in conduction band electron density goes hand in hand with the decrease in the Drude absorption. However, STEs can serve as an additional source for the creation of free electrons on the time scale of the laser interaction and eventually contribute to the energy transfer to the lattice on time scales of a few hundreds of picoseconds [18,19].

This means that the STEs play an important role for all pulses longer than 150 fs. To take advantage of this, an optimized pulse sequence consists of a short and intense pulse followed by a long, low-intensity part. The short pulse is intense enough to excite a significant number of electrons into the conduction band, well below the critical electron density. This allows the laser pulse to penetrate deeply into the material. Shortly after the excitation, the electrons are stored in STEs and are ready for a re-excitation by lower intensities, as those states are located within the bandgap. This is realized by the low-intensity part of the ideal pulse sequence. This re-excitation process might be repeated several times until the energy density for ablation is reached. In order to limit effects due to heat diffusion, the overall pulse sequence should be in the range of a few picoseconds. Temporal pulse shapes that mimic the optimal behavior can be synthesized with the help of spectral phase modulation [20]. In a Taylor expansion of the spectral phase, the third term φ_3 leads to third-order dispersion (TOD). Mathematically, the temporal pulse envelope

is described by the product of an Airy function and an exponential decay [21]. This is why we refer to these pulses as TAPs. Pulses with positive φ_3 start with an intense main pulse followed by a pulse sequence with decreasing intensity [see the upper panel of Fig. 2(d)].

Increasing φ_3 enlarges the pulse duration as well as the temporal asymmetry, whereas the instantaneous frequency remains constant. In contrast, modulation with the second-order term φ_2 leads to group delay dispersion (GDD), which is characterized by a temporally symmetric intensity profile [see the upper panel of Fig. 2(e)] and a linear sweep of the instantaneous frequency. An increase in φ_2 also leads to an elongated pulse duration. A detailed mathematical description can be found in Wollenhaupt *et al.* [21,22].

In our experiments, we focus linearly polarized femtosecond laser pulses with a central wavelength $\lambda = 785$ nm under ambient conditions with a long distance microscope objective (NA = 0.5) above, on, and below a fused silica surface [Figs. 1 and 2(a)] with a bandgap of $E_{\text{gap,VB}} = 9$ eV [23]. Three different pulse shapes are used: bandwidth-limited pulses of 30 fs duration, TAPs with increasing TOD, where the statistical pulse duration [21] increases from 260 fs for $\varphi_3 = 1 \times 10^5$ fs³ via 770 fs for $\varphi_3 = 3 \times 10^5$ fs³ to 1.5 ps for $\varphi_3 = 6 \times 10^5$ fs³, and temporally symmetric pulses with a duration of about 1.4 ps ($\varphi_2 = 1.5 \times 10^4$ fs²), matching the statistical pulse duration of the longest TAP. For each pulse shape, the fluence is 2.5 times above the corresponding damage threshold ($2.5 \times E_{\text{thr}}$). In addition, ablation structures resulting from the longest TAPs are compared to structures of a bandwidth-limited pulse at the same fluence. The results for selected pulse shapes are displayed and compared to simulations in Fig. 2. The upper panels show the relative intensity profile of each pulse with respect to the bandwidth-limited pulse at a fluence of $2.5 \times E_{\text{thr}}$ [Fig. 2(b)]. In the simulations the excitation and recombination dynamics in the direction of laser propagation (z -axis) are calculated via rate equations, taking the electron density in the conduction, valence, and trapping bands as well as the total electron density into account (for details, see Supplement 1).

3. EXPERIMENTAL SETUP

The experimental setup is sketched in Fig. 1. Laser pulses of 30 fs duration (FWHM) at a central wavelength of 785 nm are provided by an amplified Ti:sapphire laser system (Femtolasers Femtopower Pro). Single pulse selection is achieved via the Pockels cell of the amplifier. Before entering the material processing platform, the pulses are guided through our high-precision home-built pulse shaper [24]. The pulse shaper is used in a “phase-only modulation” mode, and the overall dispersion of optical elements up to the sample surface is coarsely compensated with the help of a commercial acousto-optic pulse shaper (Dazzler) contained in the amplifier and fine adjusted with the home-built pulse shaper prior to applying the required phase functions. Temporal pulse characterization of selected pulse shapes was performed via cross-correlation measurements directly in the interaction region. The linearly polarized and temporally shaped laser pulses are focused on a UV-grade fused silica sample (Spectrosil 2000) using a microscope objective (Zeiss LD Epiplan 50×/0.50 NA) with a 7 mm working distance. The $1/e^2$ intensity spot radius was measured using a knife-edge method, and the obtained value of 1 μm was applied in the simulations. The

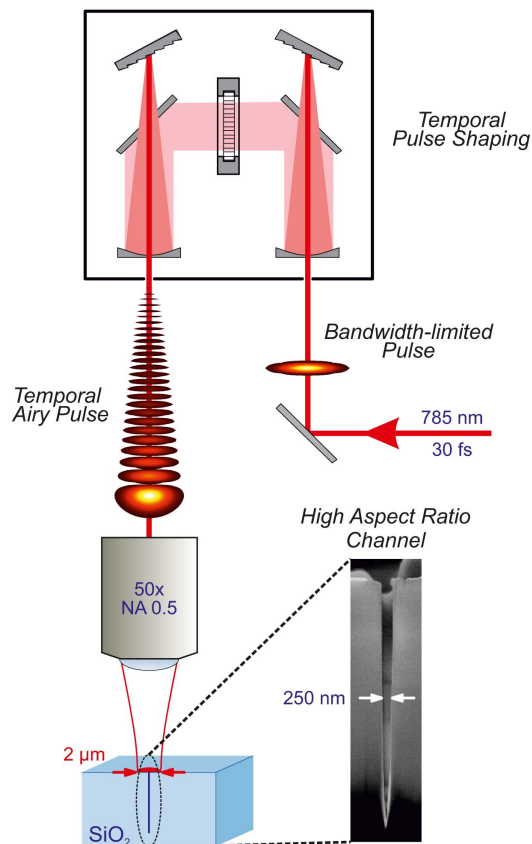


Fig. 1. Schematic of the experimental setup for generating high aspect ratio nanochannels in fused silica together with a scanning electron micrograph of a created high aspect ratio channel (lower right). The measured spot diameter of $2\ \mu\text{m}$ is indicated by the red arrows on the sample.

calculated Rayleigh length for the measured spot radius is $4\ \mu\text{m}$. The sample is translated by a three-axis piezo table for each pulse exposure. The focal position is changed in steps of $\Delta z = 1\ \mu\text{m}$ for fixed pulse energy and pulse shape. After laser processing and cleaning, the samples are analyzed by cross-section cutting with FIB followed by scanning electron microscopy imaging.

4. MACHINING RESULTS AND HIGH ASPECT RATIO FORMATION

The machining results for bandwidth-limited pulses at $100\ \text{nJ}$ ($2.5 \times E_{\text{thr}}$) pulse energy are displayed in Fig. 2(b). Shallow ablation structures are created for all focal positions. When the pulse energy is increased to $250\ \text{nJ}$, the hole depth stagnates, as can be seen in Fig. 2(c).

This observation changes when fused silica is processed with shaped laser pulses. When the temporal pulse shape is tailored to the abovementioned asymmetric [Fig. 2(d)] and symmetric [Fig. 2(e)] intensity distributions with pulse lengths of 1.5 and $1.4\ \text{ps}$, respectively, hole structures with a huge aspect ratio (hole depth to channel width) up to $30:1$ are observed. The hole depth of each pulse shape and the focusing position are well reproduced in the simulations. We observe that the deeper the laser focus is located inside the bulk material, the longer the ablation structure is.

For asymmetric pulses, the channel width of the ablation structures is in the range of $200\text{--}350\ \text{nm}$, and therefore well below the $785\ \text{nm}$ wavelength. A decrease in the temporal

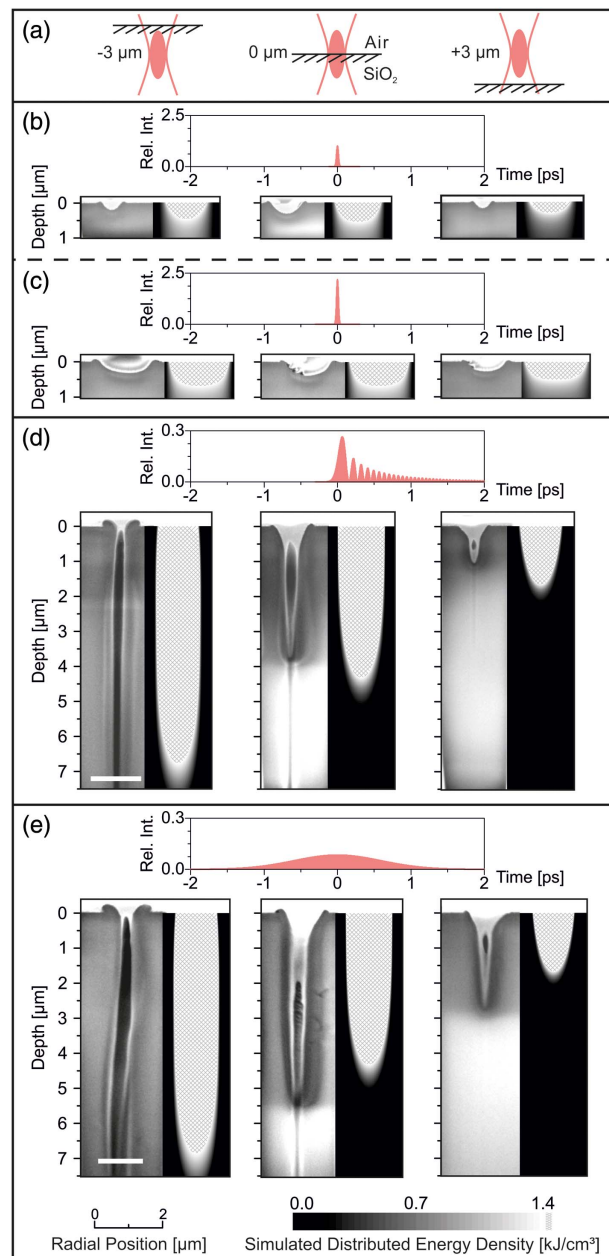


Fig. 2. Machining results for (b), (c) bandwidth-limited pulses, (d) TAPs with $\varphi_3 = 6 \times 10^5\ \text{fs}^3$, and (e) temporally symmetric pulses with $\varphi_2 = 1.5 \times 10^4\ \text{fs}^2$ at three different focus positions with respect to the surface of the fused silica sample as indicated in (a). For each focus position, scanning electron microscope images of cross-sections obtained by FIB milling (left) are compared to simulations (right). Experiments in (b), (d), and (e) were performed at approximately $2.5 \times E_{\text{thr}}$ for the corresponding pulse shape. Results for bandwidth-limited pulses approximately 6 times above their threshold and corresponding to the same pulse energy as used for shaped pulses in (d) are displayed in (c) showing shallow structures. The peak intensities of the applied pulses in the pulse pictograms are normalized to the simulated bandwidth-limited pulse shown in (b). The dark shaded areas close to the hole in the scanning electron microscope images are attributed to densified material after material processing. Vertical white lines in the middle column in (d) and (e) are FIB milling artifacts, and horizontal white bars in (d) and (e) indicate the measured hole depth.

asymmetry, accompanied by a shorter temporal pulse duration, leads to a decrease in the hole depth and aspect ratio, as presented in Figs. 3(a)–3(c).

For symmetric pulses, the same depth is reached; however, larger diameters and irregularities are observed. The mechanisms responsible for the irregularities have not been identified so far. These pulses seem to be less robust with respect to high aspect ratio machining.

Figure 3 summarizes the hole depths in the experiment and the simulation and the aspect ratio achieved with respect to the focus position for increasing the temporal asymmetry and

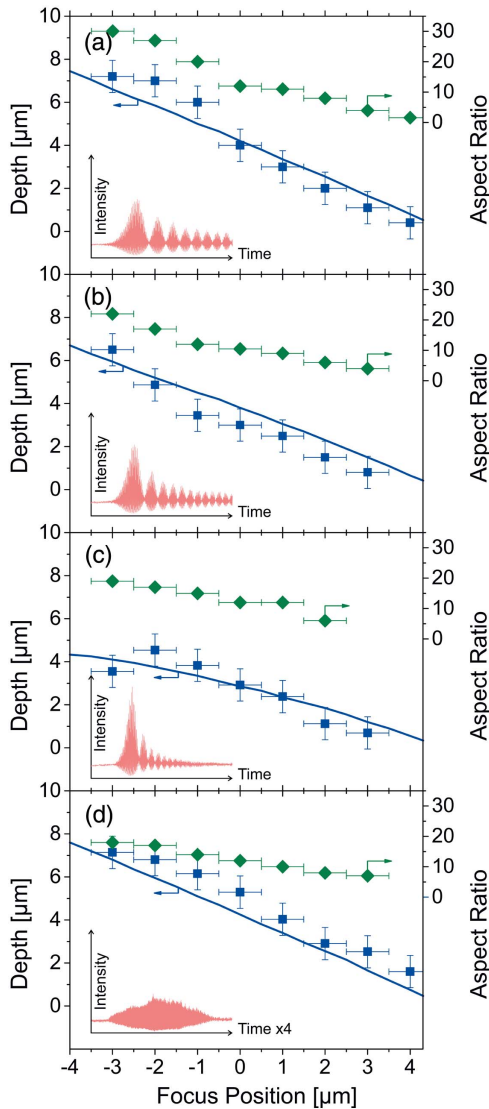


Fig. 3. Experimental hole depth (blue squares), simulated hole depth (solid blue line), and measured aspect ratio (green diamonds) with respect to focus position (minus/plus: focus below/above surface) for four different pulse shapes. (a)–(c) TAP shapes with decreasing TOD parameter and correspondingly decreasing statistical pulse duration [(a) $\varphi_3 = 6 \times 10^5 \text{ fs}^3$; 1.5 ps, (b) $\varphi_3 = 3 \times 10^5 \text{ fs}^3$; 770 fs, (c) $\varphi_3 = 1 \times 10^5 \text{ fs}^3$; 260 fs], where the pulse duration in (a) corresponds to the data in Fig. 2(d). (d) Temporally symmetric pulse shape with $\varphi_2 = 1.5 \times 10^4 \text{ fs}^2$ (1.4 ps pulse duration) corresponding to the data shown in Fig. 2(e). Each set was recorded with a pulse energy $2.5 \times E_{\text{thr}}$. All analyzed pulse shapes are identified by cross-correlation measurements and included as insets in (a)–(d). All cross-correlations are normalized in intensity. The time axes in (a)–(c) are shown for a range of 1 ps, whereas it is 4 ps in (d). Error bars stem from an inaccuracy of $\pm 0.5 \mu\text{m}$ for the focus position and from postmortem hole depth analysis. The aspect ratio is calculated as the hole depth divided by the full channel width at half depth.

the symmetric pulse profile. In addition, cross-correlations of temporal pulse shapes, measured directly in the interaction region, are displayed.

5. DISCUSSION

Bandwidth-limited pulses have a significantly higher peak intensity than elongated temporally shaped pulses for the same pulse energy. Even when setting the same relative pulse energies with respect to E_{thr} , the bandwidth-limited pulse still has a peak intensity approximately 3 times higher than that of a TAP with $\varphi_3 = 6 \times 10^5 \text{ fs}^3$ [Figs. 2(b) and 2(d)]. At these high laser intensities, air close to the target will be excited, since the ionization potential of air $E_{\text{gap,air}} = 14.6 \text{ eV}$ is only $1.6 \times E_{\text{gap,CB}}$ of fused silica. This leads to a significant absorption [25] of the laser pulse before it reaches the surface of the sample, limiting the energy input into the material. In our simulations, we included absorption in air for bandwidth-limited pulses based on results from Liu *et al.* [26]. In addition, bandwidth-limited laser pulses of 30 fs create a very high conduction band electron density within the first few hundreds of nanometers that will lead to a rapid and strong absorption and reflection of the laser pulse, suppressing energy deposition beyond this distance. As the maximum temporal intensity of the pulse has passed, the conduction band electron density $N_{\text{CB}}(t)$ strongly decreases due to the fast trapping mechanism of 150 fs [11] into exciton states ($E_{\text{gap,TB}} = 5.2 \text{ eV}$ [23]), as illustrated in Fig. 4(b). Free carrier absorption in air and inside the sample due to a high conduction band electron density is one mechanism leading to stagnation of the hole depth. Stagnation from absorption due to strong field excitation [27] is not considered in our simulations.

In comparison to bandwidth-limited laser pulses, temporally shaped pulses—either symmetrically or asymmetrically—interact with the material in a different fashion. Their low peak intensities avoid absorption in air as well as strong absorption close to the surface. Thus, these pulses are able to provide more energy for the excitation in the depth of the material, which might be sufficient for material ablation. The temporal structure of the asymmetric pulse is furthermore responsible for the characteristic interplay of trapping and re-excitation of electrons ending in an oscillating behavior of $N_{\text{CB}}(t)$ [Fig. 4(c)], showing that there is still an observable energy deposition after 2.5 ps. The maximum $N_{\text{CB}}(t)$ is much lower than for bandwidth-limited pulses, even though the same deposited energy of $W = 1.4 \frac{\text{kJ}}{\text{cm}^2}$ is accomplished at the end of the pulse [Fig. 4(a)]. As listed in Table S1 of Supplement 1, it is noteworthy within this context that 52% (36% for the symmetric and less than 1% for the bandwidth-limited pulse) of the energy required for ablation is discharged into the material by the re-excitation of STEs via MPI and mainly AI. As a consequence, the energy deposition takes place in a confined region, because the re-excited STEs are localized close to a single SiO_2 complex [11].

Regarding the subwavelength dimensions of the hole structures, we note that not all critically excited material can be ejected during the ablation process. This is supported by the rims formed close to the craters. The rims are not significantly larger for temporally shaped laser pulses than for holes generated by bandwidth-limited pulses, as shown in Fig. 2. As the excited material is nearly completely enclosed by the unexcited material, high pressure inside the material can lead to the formation of super dense material phases arising during the excitation and ablation process and ending in densified material close to the channel crater. This

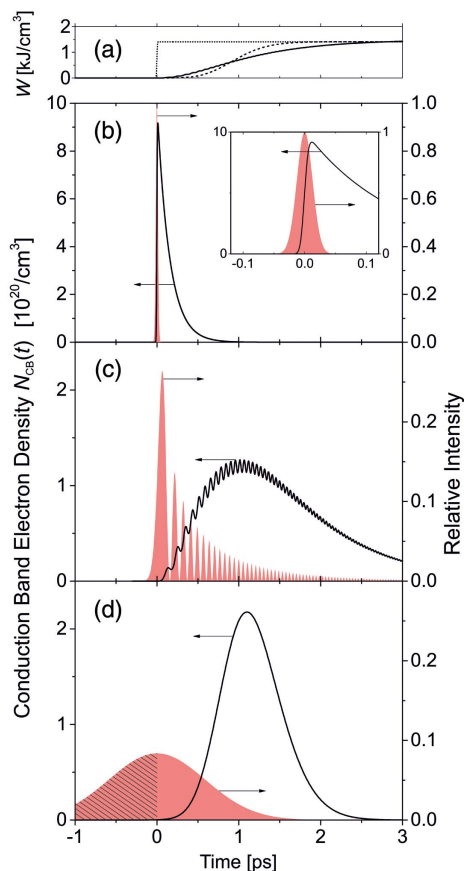


Fig. 4. (a) Cumulative simulated time-dependent total energy density W transferred to the fused silica sample for bandwidth-limited pulses (dotted line), TAPs with a TOD of $\varphi_3 = 6 \times 10^5 \text{ fs}^3$ (solid line), and temporally symmetric pulses with $\varphi_2 = 1.5 \times 10^4 \text{ fs}^2$ (dashed line), each at their corresponding ablation threshold E_{thr} . For all pulse shapes the same accumulated energy density of $W_{\text{cr}} = 1.4 \frac{\text{kJ}}{\text{cm}^2}$ has been transferred at the end of the laser pulse. (b)–(d) Simulated time-dependent conduction band electron density (black line) in the first layer (1 nm) below the surface in the center of the laser pulse for (b) bandwidth-limited pulses, (c) TAPs with $\varphi_3 = 6 \times 10^5 \text{ fs}^3$, and (d) GDD-shaped laser pulses with $\varphi_2 = 1.5 \times 10^4 \text{ fs}^2$, each at their corresponding ablation threshold. The intensities of the temporal pulse shapes (red shaded, right y-axis) are normalized to the bandwidth-limited pulse in (b). Note the different plot range for (b) for conduction band electron density and the temporal close-up of the pulse shape. The black shaded area in (d) shows the part of the intensity that does not contribute to the ablation energy density.

was recently observed in the case of void formations in fused silica [28] and silicon [29]. In addition, it was recently found that laser excitation in water by TAP pulses is distributed over a strongly reduced area and greater depth compared to ultrashort bandwidth-limited laser pulses [30].

For temporally symmetrically shaped pulses, the ablation threshold is approximately 1.8 times higher compared to the that of asymmetrically shaped ones (178 versus 100 nJ; see Table S1 of Supplement 1) due to the even lower peak intensity. In this case, almost the first half of the pulse is not intense enough to excite a significant number of initial seed electrons for AI, as indicated by the shaded area in Fig. 4(d). In addition, Fig. 4(a) shows the accumulated energy density over time, which starts to increase after time zero, showing that the second half of the pulse mainly provides the energy for ablation. For higher pulse energies, the onset

of absorption will be shifted toward earlier parts of the pulse, but a significant fraction of the pulse will still be unused for excitation. In the end, the absorbed part of the temporally symmetric pulse is a temporally asymmetric shape. As mentioned above, this is reflected in the very similar temporal dependences of the accumulated energy density for both shaped pulses, as shown in Fig. 4(a).

Regarding the slightly larger channel width, we assume that the continuous heating of the conduction band electrons results in a high average kinetic energy, causing a distribution of electrons over a larger volume. The consequence is supposed to be an extended affected zone of deposited energy and therefore an increased channel width, resulting in a smaller aspect ratio for temporally symmetrically shaped pulses.

This is supported by Fig. 4(d). On one hand, the maximum $N_{\text{CB}}(t)$ is clearly larger than for TAPs, and no oscillations within $N_{\text{CB}}(t)$ can be observed. On the other hand, the maximum $N_{\text{CB}}(t)$ is noticeably smaller than for bandwidth-limited pulses, due to the smaller peak intensity and the electron trapping. As mentioned above, the re-excitation of STEs contributes noticeably to W with about 36% (Table S1 of Supplement 1), which is attributed to the elongation of the pulse in time.

In the end, all this also manifests in a high penetration depth [Fig. 3(d)] for temporally symmetric shaped pulses, albeit with much lower efficiency and smaller aspect ratios.

A direct comparison of the experiment and simulation in Fig. 2 shows that on one hand the hole depths are in very good agreement, while on the other hand the channel width could be less well reproduced. This is related to the obvious limitations of the simulation, which includes neither the energy transfer to the lattice nor subsequent phase transitions, as discussed above.

To estimate the limits of the presented temporal pulse shaping technique, we simulated the maximum depth in the simulations for focusing at the surface. We increased the power for the TAP with $\varphi_3 = 6 \times 10^5 \text{ fs}^3$ to $33.3 \times E_{\text{thr}}$ (Table S3 of Supplement 1), reaching the critical power for self-focusing. The simulated ablation depth of $15.5 \mu\text{m}$ is more than 4 times larger than the Rayleigh range. In terms of the temporal asymmetry and pulse duration, we increased the TOD parameter to $\varphi_3 = 2 \times 10^6 \text{ fs}^3$, with a corresponding pulse duration of 5.1 ps. The simulated hole depth for $2.5 \times E_{\text{thr}}$ is around $4.7 \mu\text{m}$, which is only slightly deeper than for $\varphi_3 = 6 \times 10^5 \text{ fs}^3$. However, the higher the temporal asymmetry and pulse duration, the more energy it takes until the critical power for self-focusing is reached compared to a low TOD parameter and shorter pulse durations. Furthermore, the simulations show that the channel diameter is nearly constant over the Rayleigh length. Thus, focusing below the surface can double the range, as seen in Fig. 2(d).

Note that similar observations have been reported using pulse durations of about 0.5 ps [31]. However, as discussed above, a large fraction of the pulse energy does not contribute to the ablation process for temporally symmetric laser pulses.

Other approaches [32–36] in which the resulting dimensions of the structures are comparable to ours apply powers well above the critical power with similar numerical apertures, and thus nonlinear propagation effects become appreciable, like self-focusing and filamentation [37]. In these investigations the laser pulses are either focused into the bulk with multipulse irradiation [32] or onto the surface with single laser pulses [33]. In the latter case, spherical aberrations are also used to elongate the focal region in the propagation direction. However, for similar hole depths and

aspect ratios, pulse energies approximately 1 order of magnitude higher are required. A second method for high aspect channel generation is the utilization of spatial pulse shaping techniques, leading to nondivergent Bessel beams, which may exceed the critical power for self-focusing. Long and thin conical profiles with a very high aspect ratio of a secondary crater in borosilicate glass were observed due to spontaneous reshaping of the incoming Gaussian pulse into a Gaussian–Bessel pulse [34], and nanochannel arrays with Bessel beams, focused onto the backside of the material generated via a virtual axicon, were presented as well [35]. It was also demonstrated that temporal stretching of the laser pulse can be beneficial for energy deposition into the material with Bessel beams [36].

Indeed, we show that temporally asymmetric pulse shaping can be utilized for the generation of nanochannels as a temporal analog to spatial pulse shaping like Bessel beams. However, the important point is that for TAP, much less pulse energy is required and all resulting high aspect structures are generated with single laser pulses well below the threshold for self-focusing.

In general, we expect that temporally shaped pulses will also create deeper structures in dielectric materials without a fast trapping mechanisms, as this simple “seed and heat” picture is valid in those materials as well [17,30,31,38].

Just as in the case of fused silica, the earlier part of an elongated pulse will create an electron density well below the damage threshold, leading to moderate absorption. Since the remaining part of the pulse will increase the conduction band electron density step by step, the parts with low intensity at the end of the pulse are affected most from the absorption. In any case, we expect that TAPs will be the most efficient choice for the generation of nanochannels, because nearly the entire pulse contributes to the excitation and nearly no energy is wasted compared to long temporally symmetric laser pulses. The latter aspect could be important in laser machining with competing absorption processes.

Within this context we note that in sapphire, a dielectric material with no distinctive trapping bands, TAPs are able to generate structures with a higher aspect ratio than bandwidth-limited pulses, as was recently demonstrated by Hernandez-Rueda *et al.* [38]. In that study, the resulting ablation structures were evaluated by atomic force microscopy (AFM). However, in the case of a high aspect ratio and narrow ablation structures with dimensions close to the AFM tip, the resolution of that technique is limited and might not be able to indicate the real depth. To verify this prediction, postmortem analysis providing full spatial information is a fitting approach.

6. SUMMARY AND CONCLUSION

We demonstrated the efficient generation of uniform high aspect ratio ablation structures in fused silica utilizing single-shot TAPs in a regime where the chosen intensity was well below the threshold for self-focusing and thus filamentation. Neither spatial beam shaping methods nor nondivergent beam propagation techniques were applied.

TAPs consist of a short and intense pulse where the peak intensity is well below the intensity needed to create a critical electron density and therefore penetrate deep into the material. The energy density needed for ablation is reached with the trailing part of the laser pulse, making use of AI and a continuous re-excitation of STEs. Heat diffusion is limited by restricting the overall pulse duration to a few picoseconds. Under moderate focusing

conditions ($NA = 0.5$), this results in high aspect ratio ablation structures ($\sim 30:1$) with channel widths in the range of a few hundred nanometers. Similar ablation structures with lower aspect ratios were obtained for temporally comparable but symmetrically shaped pulses; however, approximately twice as much pulse energy was required. Furthermore, we controlled the structure depth by tuning the asymmetry, i.e., the pulse duration, of the temporally shaped laser pulses: the more pronounced the asymmetry and the longer the pulse duration, the deeper the structures.

An adapted simplified rate equation model (see Supplement 1) has been developed as supporting evidence. Numerical simulations and experimental results show good agreement with respect to hole depth.

We argue that similar mechanisms could be exploited in other dielectric materials as well. Hence, our results enable a fast processing technique for tailored design in several optical and photonic applications as well as for implementations in nanosurgery.

Funding. Deutsche Forschungsgemeinschaft (DFG) (SPP1327).

Acknowledgment. The authors thank Matthias Wollenhaupt for fruitful discussions in an initial phase of the experiment and Lasse Haahr-Lillevang for discussions on the simulations. Advice from Jens Köhler regarding pulse shaping is also gratefully acknowledged. T. W. thanks the Otto Braun Fund for a Ph.D. scholarship.

See Supplement 1 for supporting content.

REFERENCES

1. J. Baglin, “Ion beam nanoscale fabrication and lithography—a review,” *Appl. Surf. Sci.* **258**, 4103–4111 (2012).
2. M. N. Hossain, J. Justice, P. Lovera, B. McCarthy, A. O’Riordan, and B. Corbett, “High aspect ratio nano-fabrication of photonic crystal structures on glass wafers using chrome as hard mask,” *Nanotechnology* **25**, 355301 (2014).
3. K. Sugioka, M. Meunier, and A. Piqué, *Laser Precision Microfabrication* (Springer, 2010).
4. P. Ronchi, S. Terjung, and R. Pepperkok, “At the cutting edge: applications and perspectives of laser nanosurgery in cell biology,” *Biol. Chem.* **393**, 235–248 (2012).
5. S. H. Chung and E. Mazur, “Surgical applications of femtosecond lasers,” *J. Biophoton.* **2**, 557–572 (2009).
6. R. Stoian, M. Wollenhaupt, T. Baumert, and I. V. Hertel, “Temporal pulse tailoring in ultrafast laser manufacturing technologies,” in *Laser Precision Microfabrication*, R. Hull, C. Jagadish, R. M. Osgood, J. Parisi, Z. Wang, and H. Warlimont, eds. (Springer, 2010), pp. 121–144.
7. M. Wollenhaupt and T. Baumert, “Ultrafast laser control of electron dynamics in atoms, molecules and solids,” *Faraday Discuss. Chem. Soc.* **153**, 9–26 (2011).
8. P. Balling and J. Schou, “Femtosecond-laser ablation dynamics of dielectrics: basics and applications for thin films,” *Rep. Prog. Phys.* **76**, 036502 (2013).
9. B. C. Stuart, M. D. Feit, A. M. Rubenchik, B. W. Shore, and M. D. Perry, “Laser-induced damage in dielectrics with nanosecond to subpicosecond pulses,” *Phys. Rev. Lett.* **74**, 2248–2251 (1995).
10. B. Chimier, O. Uteza, N. Sanner, M. Sentis, T. Itina, P. Lassonde, F. Legare, F. Vidal, and J. C. Kieffer, “Damage and ablation thresholds of fused-silica in femtosecond regime,” *Phys. Rev. B* **84**, 094104 (2011).
11. S. S. Mao, F. Quéré, S. Guizard, X. Mao, R. E. Russo, G. Petite, and P. Martin, “Dynamics of femtosecond laser interactions with dielectrics,” *Appl. Phys. A* **79**, 1695–1709 (2004).

12. C. Sarpe, J. Köhler, T. Winkler, M. Wollenhaupt, and T. Baumert, "Real-time observation of transient electron density in water irradiated with tailored femtosecond laser pulses," *New J. Phys.* **14**, 075021 (2012).
13. I. H. Chowdhury, X. Xu, and A. M. Weiner, "Ultrafast double-pulse ablation of fused silica," *Appl. Phys. Lett.* **86**, 151110 (2005).
14. C. Sarpe-Tudoran, A. Assion, M. Wollenhaupt, M. Winter, and T. Baumert, "Plasma dynamics of water breakdown at a water surface induced by femtosecond laser pulses," *Appl. Phys. Lett.* **88**, 261109 (2006).
15. V. V. Temnov, K. Sokolowski-Tinten, P. Zhou, A. El-Khamhawy, and D. von der Linde, "Multiphoton ionization in dielectrics: comparison of circular and linear polarization," *Phys. Rev. Lett.* **97**, 237403 (2006).
16. L. Englert, B. Rethfeld, L. Haag, M. Wollenhaupt, C. Sarpe-Tudoran, and T. Baumert, "Control of ionization processes in high band gap materials via tailored femtosecond pulses," *Opt. Express* **15**, 17855–17862 (2007).
17. L. Englert, M. Wollenhaupt, C. Sarpe, D. Otto, and T. Baumert, "Morphology of nanoscale structures on fused silica surfaces from interaction with temporally tailored femtosecond pulses," *J. Laser Appl.* **24**, 042002 (2012).
18. S. Richter, M. Heinrich, S. Döring, A. Tünnermann, and S. Nolte, "Nanogratings in fused silica: formation, control, and applications," *J. Laser Appl.* **24**, 042008 (2012).
19. S. Höhm, A. Rosenfeld, J. Krüger, and J. Bonse, "Femtosecond diffraction dynamics of laser-induced periodic surface structures on fused silica," *Appl. Phys. Lett.* **102**, 054102 (2013).
20. A. M. Weiner, "Ultrafast optical pulse shaping: a tutorial review," *Opt. Commun.* **284**, 3669–3692 (2011).
21. M. Wollenhaupt, L. Englert, A. Horn, and T. Baumert, "Temporal femtosecond pulse tailoring for nanoscale laser processing of wide-bandgap materials," *Proc. SPIE* **7600**, 76000X (2010).
22. M. Wollenhaupt, L. Englert, A. Horn, and T. Baumert, "Control of ionization processes in high band gap materials," *J. Laser Micro/Nanoeng.* **4**, 144–151 (2009).
23. N. M. Bulgakova, R. Stoian, and A. Rosenfeld, "Laser-induced modification of transparent crystals and glasses," *Quantum Electron.* **40**, 966–985 (2010).
24. J. Köhler, M. Wollenhaupt, T. Bayer, C. Sarpe, and T. Baumert, "Zeptosecond precision pulse shaping," *Opt. Express* **19**, 11638–11653 (2011).
25. N. M. Bulgakova, V. P. Zhukov, A. R. Collins, D. Rostohar, T. J.-Y. Derrien, and T. Mocek, "How to optimize ultrashort pulse laser interaction with glass surfaces in cutting regimes?" *Appl. Surf. Sci.* **336**, 364–374 (2015).
26. X. L. Liu, X. Lu, X. Liu, T. T. Xi, F. Liu, J. L. Ma, and J. Zhang, "Tightly focused femtosecond laser pulse in air: from filamentation to breakdown," *Opt. Express* **18**, 26007–26017 (2010).
27. K. Waedegaard, M. Frislev, and P. Balling, "Femtosecond laser excitation of dielectric materials: experiments and modeling of optical properties and ablation depths," *Appl. Phys. A* **110**, 601–605 (2013).
28. E. G. Gamaly, L. Rapp, V. Roppo, S. Juodkazis, and A. V. Rode, "Generation of high energy density by fs-laser-induced confined micro-explosion," *New J. Phys.* **15**, 025018 (2013).
29. L. Rapp, B. Haberl, C. J. Pickard, J. E. Bradby, E. G. Gamaly, J. S. Williams, and A. V. Rode, "Experimental evidence of new tetragonal polymorphs of silicon formed through ultrafast laser-induced confined micro-explosion," *Nat. Commun.* **6**, 7555 (2015).
30. T. Winkler, C. Sarpe, N. Jelzow, L. H. Lillevang, N. Götte, B. Zielinski, P. Balling, A. Sentfleben, and T. Baumert, "Probing spatial properties of electronic excitation in water after interaction with temporally shaped femtosecond laser pulses: experiments and simulations," *Appl. Surf. Sci.*, doi: 10.1016/j.apsusc.2015.11.182 (to be published).
31. J. F. Herbstman and A. J. Hunt, "High-aspect ratio nanochannel formation by single femtosecond laser pulses," *Opt. Express* **18**, 16840–16848 (2010).
32. A. Couairon, L. Sudrie, M. Franco, B. Prade, and A. Mysyrowicz, "Filamentation and damage in fused silica induced by tightly focused femtosecond laser pulses," *Phys. Rev. B* **71**, 125435 (2005).
33. Y. V. White, X. Li, Z. Sikorski, L. M. Davis, and W. Hofmeister, "Single-pulse ultrafast-laser machining of high aspect nano-holes at the surface of SiO₂," *Opt. Express* **16**, 14411–14420 (2008).
34. B. Delobelle, R. Salut, F. Courvoisier, and P. Delobelle, "A detailed study through the focal region of near-threshold single-shot femtosecond laser ablation nano-holes in borosilicate glass," *Opt. Commun.* **284**, 5746–5757 (2011).
35. M. K. Bhuyan, F. Courvoisier, P. A. Lacourt, M. Jacquot, R. Salut, L. Furfaro, and J. Dudley, "High aspect ratio nanochannel machining using single shot femtosecond Bessel beams," *Appl. Phys. Lett.* **97**, 081102 (2010).
36. M. K. Bhuyan, P. K. Velpula, J. P. Colombier, T. Olivier, N. Faure, and R. Stoian, "Single-shot high aspect ratio bulk nanostructuring of fused silica using chirp-controlled ultrafast laser Bessel beams," *Appl. Phys. Lett.* **104**, 021107 (2014).
37. A. Couairon and A. Mysyrowicz, "Femtosecond filamentation in transparent media," *Phys. Rep.* **441**, 47–189 (2007).
38. J. Hernandez-Rueda, N. Götte, J. Siegel, M. Soccio, B. Zielinski, C. Sarpe, M. Wollenhaupt, T. A. Ezquerro, T. Baumert, and J. Solis, "Nanofabrication of tailored surface structures in dielectrics using temporally shaped femtosecond-laser pulses," *ACS Appl. Mater. Interface* **7**, 6613–6619 (2015).

Temporal Airy pulses for controlled high aspect ratio nanomachining of dielectrics: supplementary material

NADINE GÖTTE,¹ THOMAS WINKLER,¹ TAMARA MEINL,² THOMAS KUSSEROW,²
 BASTIAN ZIELINSKI,¹ CRISTIAN SARPE,¹ ARNE SENFTLEBEN,¹ HARTMUT HILLMER,²
 THOMAS BAUMERT,^{1,*}

¹University of Kassel, Institute of Physics and CINSaT, Heinrich-Plett-Str. 40, 34132 Kassel, Germany

²University of Kassel, Institute of Nanostructure Technologies and Analytics and CINSaT, Heinrich-Plett-Str. 40, 34132 Kassel, Germany

*Corresponding author: baumert@physik.uni-kassel.de

Published 5 April 2016

This document contains supplementary information on rate equation simulations for “Temporal Airy pulses for controlled high aspect ratio nanomachining of dielectrics” <http://dx.doi.org/10.1364/optica.3.000389>. © 2016

Optical Society of America

<http://dx.doi.org/10.1364/optica.3.000389.s001>

1. Rate equations

We simulate the temporal laser intensity-dependent $I(t)$ excitation and recombination dynamics in the direction of laser propagation (z -axis) via the following rate equations:

$$\begin{aligned} \frac{\partial N_{CB}(t)}{\partial t} &= \left(\frac{N_{VB}(t)}{N_{tot}} \right) \cdot (\sigma_{VB} \cdot I(t)^6 + \alpha_{VB} \cdot N_{CB}(t_{ret-9}) \cdot I(t)) + \left(\frac{N_{TB}(t)}{N_{tot}} \right) \cdot (\sigma_{TB} \cdot I(t)^4 + \alpha_{TB} \cdot N_{CB}(t_{ret-5}) \cdot I(t)) - \frac{N_{CB}(t)}{t_T} \\ \frac{\partial N_{TB}(t)}{\partial t} &= \left(\frac{N_{TB}(t)}{N_{tot}} \right) \cdot (\sigma_{TB} \cdot I(t)^4 + \alpha_{TB} \cdot N_{CB}(t_{ret-5}) \cdot I(t)) + \frac{N_{CB}(t)}{t_T} \end{aligned} \quad (S1)$$

Where $N_{CB}(t)$, $N_{VB}(t)$, $N_{TB}(t)$, N_{tot} are the time-dependent electron density in the conduction, valence, trapping band and the total (excitable) valence electron density; σ_{VB} , σ_{TB} (α_{VB} , α_{TB}) are the multiphoton (avalanche) coefficients for excitation from the valence band and trapping band into the conduction band, respectively; $t_T = 150$ fs is the trapping time in fused silica [1] and $t_{ret-k} = t - k \cdot \tau_{s,fix}$ is the retarded time [2],[3] for avalanche ionization with $k = 1.5 \times E_{gap} / E_{ph}$ corresponding to the number of required photons with an energy of E_{ph} for impact ionization [4],[5] and $\tau_{s,fix} = 1$ fs is a fixed electron scattering time used to calculate the retarded time [6]. This takes into account that a conduction band electron requires a finite time to reach the critical energy for impact ionization [5],[3] due to several single photon absorption and scattering events. Relaxation processes from the trapping to the valence band take place on a much longer timescale of a few hundreds of picoseconds [7],[8] and are thus neglected.

As we concentrate our studies to an excitation regime, where tunnel ionization has only a minor contribution, it is not included in our simulations. Furthermore the ponderomotive force, which causes an increase in bandgap and photonicity, is also neglected in our model.

2. Intensity evolution of the laser pulse

$I_{in}(t, r, z)$ is the time- and radial-dependent intensity that penetrates into the material and is calculated by

$$\begin{aligned} I_m(t, r, z) &= (1 - R(t, r)) \cdot I_0(t, r) \cdot \exp \left[-4 \ln 2 \cdot \left(\frac{t}{\Delta t} \right)^2 \right] \\ &\cdot \left(\frac{w_0}{w(z)} \right)^2 \cdot \exp \left[-2 \cdot \left(\frac{r}{w(z)} \right)^2 \right] \end{aligned} \quad (S2)$$

I_0 is the incident intensity at material's surface, where absorption in air for bandwidth-limited pulses is already subtracted. Absorption in air is calculated in the same way as the absorption inside the sample, however the excitation modelling is based on

results from Liu et al. [9]. $w(z) = w_0 \sqrt{1 + \left(\frac{z}{z_0}\right)^2}$ is the beam radius at a distance z to the beam waist w_0 (measured to be 1 μm) and $z_0 = \sqrt{\frac{\pi w_0^2}{\lambda}}$ is the Rayleigh length.

The reflection coefficient $R(t, r)$

$$R(t, r) = \left| \frac{n_{\text{air}} - \tilde{n}_{\text{exc}}}{n_{\text{air}} + \tilde{n}_{\text{exc}}} \right|^2 = \left| \frac{1 - \tilde{n}_{\text{exc}}}{1 + \tilde{n}_{\text{exc}}} \right|^2 \quad (\text{S3})$$

was calculated using the Fresnel equations at normal incidence in combination with the Drude model. The refractive index of air is $n_{\text{air}} = 1$ and the complex refractive index \tilde{n}_{exc} of the excited fused silica sample is defined in equation (S5). For bandwidth limited laser pulses, however, the refractive index of air is also affected by the excitation above the sample, leading to an electron density dependent expression, as in the case of fused silica. The depth-dependent laser intensity is calculated by the following differential equation in propagation direction [10]:

$$\frac{\partial I(t, z)}{\partial z} = -6 \cdot \hbar \omega \cdot \sigma_{\text{VB}} I(t, z)^6 - 4 \cdot \hbar \omega \cdot \sigma_{\text{TB}} I(t, z)^4 - \alpha' \cdot I(t, z) \quad (\text{S4})$$

The first two summands (absorption due to multiphoton ionization) are neglected as it is small in comparison to free carrier absorption in the case of the shaped laser pulses. The second term describes the Beer-Lambert absorption where $\alpha' = \frac{2\omega}{c} \cdot \text{Im} \tilde{n}$ is the absorption coefficient and $\text{Im} \tilde{n}$ the imaginary part of the complex refractive index. The complex refractive index in turn, changes as the material gets excited $\tilde{n} \rightarrow \tilde{n}_{\text{exc}}$ due to the decreasing valence band electrons. This is described by the dielectric function $\varepsilon(\omega)$ of the excited material [11] for the laser angular frequency ω based on the Drude-Model:

$$\varepsilon(\omega) = 1 + \frac{3(N_{\text{tot}} - N_{\text{CB}})\beta_{\text{CM}}}{3 - (N_{\text{tot}} - N_{\text{CB}})\beta_{\text{CM}}} - \frac{\omega_{\text{pl}}^2}{\omega^2 + i\omega/\tau_s} = \tilde{n}_{\text{exc}}^2 \quad (\text{S5})$$

The first two terms describe the contribution of the valence band electrons to the dielectric function, where β_{CM} is the Clausius-Mossotti parameter [11] chosen such that the refractive index of the unexcited material is $n = \sqrt{\varepsilon(\omega)}$ for $N_{\text{VB}} = N_{\text{tot}}$. The third term accounts for the change of the optical properties by the free electrons via the plasma frequency $\omega_{\text{pl}} = \sqrt{\frac{e^2 N_{\text{CB}}}{m_e \varepsilon_0}}$ with e and m_e as the electron charge and its corresponding effective conduction band mass, ε_0 is the vacuum permittivity. Scattering time calculation for τ_s were performed similar to Jiang and Tsai [12],[10]. A constant term for electron-phonon ($\tau_{\text{e-p}} = 1 \text{ fs}$) scattering and an electron density-dependent contribution $\tau_{\text{e-CB}}(N_{\text{CB}})$ with $\tau^* = 1 \text{ fs}$ [13] and was employed:

$$\tau_s = \left(\frac{1}{\tau_{\text{e-p}}} + \frac{1}{\tau_{\text{e-CB}}(N_{\text{CB}})} \right)^{-1} = \left(\frac{1}{\tau_{\text{e-p}}} + \frac{1}{\tau^* \cdot \frac{N_{\text{crit}}}{N_{\text{CB}}}} \right)^{-1} \quad (\text{S6})$$

Parameters for beam waist and pulse duration are taken from experimental data.

3. Determination of the parameters for simulation

One set of parameters for excitation coefficients of MPI σ and AI α for excitation from the valence ($\sigma_{\text{VB}} / \alpha_{\text{VB}}$) and trapping band ($\sigma_{\text{TB}} / \alpha_{\text{TB}}$) into the conduction band was extracted from the measured data. To that end, the parameters for all pulse shapes were fitted such that the simulated threshold energies matched the measured ones most closely (Table S1).

Table S1: Threshold values for material ablation (experiment, simulation and quotient), calculated Keldysh parameter γ [11],[15] for the peak intensity at $2.5 \times E_{\text{thr, simu}}$ and the fraction of the intensity for which $\gamma > 1$ (MPI is dominant) for each pulse shape. The last two columns indicate the fractional energy contribution for excitation from valence to conduction band (VB \rightarrow CB) and trapping to conduction band (TB \rightarrow CB) with respect to the whole excitation energy, respectively. BWL = bandwidth-limited, TOD = third order dispersion, GDD = second order dispersion.

pulse shape	E_{thr} [nJ]	$E_{\text{thr, simu}}$ [nJ]	γ @ $2.5 \times E_{\text{thr, simu}}$	fraction MPI regime ($\gamma > 1$) @ $E_{\text{thr, simu}}$	fraction VB \rightarrow CB @ $E_{\text{thr, simu}}$	fraction TB \rightarrow CB @ $E_{\text{thr, simu}}$
BWL	40	46	0.75	75%	>99%	<1%
TOD $\varphi_3 = +1 \times 10^5 \text{ fs}^3$	80	62	0.91	65%	76%	24%
TOD $\varphi_3 = +3 \times 10^5 \text{ fs}^3$	90	81	1.09	100%	58%	42%
TOD $\varphi_3 = +6 \times 10^5 \text{ fs}^3$	100	100	1.21	100%	48%	52%
GDD $\varphi_2 = +1.5 \times 10^4 \text{ fs}^2$	155	178	2.16	100%	64%	36%

Table S2: Listing of simulation parameters, which are used for numerical simulations of SiO₂. VB = valence band, CB = conduction band, TB = trapping band.

description	symbol	value	reference
refractive index in SiO ₂ @ 785 nm	n	1.4536	[16]
refractive index in air @ 785 nm	n_{air}	1	
nonlinear refractive index	n_2	$3.54 \times 10^{-16} \frac{\text{cm}^2}{\text{W}}$	[17]
central laser wavelength	λ	785 nm	
reduced electron mass in material	$0.86 m_e$	$7.83407 \times 10^{-31} \text{ kg}$	[18]
electron scattering time coefficient	τ^*	1 fs	[13]
fixed electron scattering time	$\tau_{s,\text{fix}}$	1 fs	[6]
band gap SiO ₂ (VB → CB)	$E_{\text{gap,VB}}$	9 eV	[19]
band gap SiO ₂ (TB → CB)	$E_{\text{gap,TB}}$	5.2 eV	[19]
band gap air	$E_{\text{gap,air}}$	14.6 eV	[9]
trapping time	t_T	150 fs	[1]
total (excitable) valence band electron density in SiO ₂	N_{tot}	$2.2 \times 10^{22} \frac{1}{\text{cm}^3}$	[20]
coefficient for multiphoton ionization with 6 photons from VB → CB	σ_{VB}	$1 \times 10^{-49} \frac{\text{cm}^9}{\text{W}^6 \text{s}}$	
coefficient for multiphoton ionization with 4 photons from TB → CB	σ_{TB}	$4 \times 10^{-21} \frac{\text{cm}^5}{\text{W}^4 \text{s}}$	
coefficient for AI with $k=9$ photons	α_{VB}	$2.5 \frac{\text{cm}^2}{\text{Ws}}$	best fit for different pulse shapes (this work)
coefficient for AI with $k=5$ photons	α_{TB}	$160 \frac{\text{cm}^2}{\text{Ws}}$	
critical energy deposition for ablation	W_{cr}	$1.4 \frac{\text{kJ}}{\text{cm}^3}$	

We used a critical energy density deposition of ($W_{\text{cr}} = 1.4 \text{ kJ/cm}^3$) into the material as an ablation criterion.

This value takes into account the accumulated energy which is deposited into the material due to the excitation of electrons from the valence and trapping band into the conduction band via the different excitation mechanisms (MPI and AI), respectively [14]. The energy density deposition value in our model is equivalent to the commonly used criterion in which the conduction band electron density $N_{\text{CB}}(t)$ exceeds a value of 10^{21} cm^{-3} . All parameters used are summarized in Table S2.

4. Discussion of nonlinear propagation effects

Nonlinear propagation effects like plasma defocusing are neglected as well as self-focusing and filamentation, as the longest temporal Airy pulses with third order dispersion of $\varphi_3 = +6 \times 10^5 \text{ fs}^3$ used have a power of only $P = 0.131 \text{ MW}$ for the main pulse at $2.5 \times E_{\text{thr}}$, which is one order of magnitude below the critical power for self-focusing (see Table S3).

The critical power P_{cr} for self-focusing of Gaussian beams is given by [22]:

$$P_{\text{cr}} \equiv 3.77 \frac{\lambda^2}{8\pi n n_2} \quad (\text{S7})$$

Where n is the linear and n_2 is the nonlinear index of refraction for fused silica. Values for n_2 are reported to be in the range from 2×10^{-16} to $3.54 \times 10^{-16} \text{ cm}^2/\text{W}$ [23],[20],[17],[24].

For a wavelength λ of 785 nm and the largest value for n_2 of $3.54 \times 10^{-16} \text{ cm}^2/\text{W}$ we obtain a critical power for self-focusing of

about $P_{\text{cr}} = 1.8 \text{ MW}$ and $P_{\text{nl}} = \frac{\pi^2}{4} P_{\text{cr}} = 4.4 \text{ MW}$ (according to

Couairon and Bergé [21]) as the lower limit. The power for the bandwidth-limited pulse at $2.5 \times E_{\text{thr}}$ is about $P = 3.2 \text{ MW}$ (for experimental value) and $P = 3.7 \text{ MW}$ (for simulation), respectively.

Table S3: Calculated ratio of pulse power to critical power for self-focusing and filamentation, respectively of different pulse shapes and intensities. The critical P_{fil} power for filamentation is calculated by $P_{\text{fil}} = \frac{\pi^2}{4} P_{\text{cr}} = 4.4 \text{ MW}$ according to Couairon and Bergé [21]. For temporal Airy pulses, only the contributions of the main pulse (energy E_{main} and power P_{main}) to P_{cr} and P_{fil} are considered and listed below. I_{main} corresponds to the peak intensity of the main pulse. BWL = bandwidth-limited, TOD = third order dispersion, GDD = second order dispersion.

pulse shape	threshold factor	pulse duration [fs]	pulse duration [fs] (main pulse)	energy E_{main} [nJ] (simulated)	P_{main} [MW] (main pulse)	I_{main} [TW/m ²] (main pulse)	$\frac{P_{\text{main}}}{P_{\text{cr}}}$ (main pulse)	$\frac{P_{\text{main}}}{P_{\text{fil}}}$ (main pulse)
BWL	1	30	30	46	1.472	98	0.82	0.33
	2.5	30	30	115	3.680	244	2.05	0.83
	5.4	30	30	250	8.000	531	4.45	1.80
TOD $\varphi_3 = +6 \times 10^5 \text{ fs}^3$	1	1539	221	12	0.053	26	0.03	0.01
	2.5	1539	221	30	0.131	64	0.07	0.03
TOD $\varphi_3 = +3 \times 10^5 \text{ fs}^3$	1	770	88	15	0.163	32	0.09	0.04
	2.5	770	88	37	0.409	79	0.23	0.09
TOD $\varphi_3 = +1 \times 10^5 \text{ fs}^3$	1	260	63	21	0.319	44	0.18	0.07
	2.5	260	63	52	0.797	111	0.44	0.18
GDD $\varphi_2 = +1.5 \times 10^4 \text{ fs}^2$	1	1387	1387	178	0.123	8	0.07	0.03
	2.5	1387	1387	445	0.308	20	0.17	0.07

Even at an applied pulse energy of 250 nJ, where the incoming power of $P = 8 \text{ MW}$ exceeds the critical power for filamentation by a factor of approx. 2 (see Table S3), no filament-like structures

could be observed by applying bandwidth-limited pulses (compare Figure 2).

References

- S. S. Mao, F. Quéré, S. Guizard, X. Mao, R. E. Russo, G. Petite, and P. Martin, "Dynamics of femtosecond laser interactions with dielectrics," *Appl. Phys. A* **79**, 1695–1709 (2004).
- C. Sarpe, J. Köhler, T. Winkler, M. Wollenhaupt, and T. Baumert, "Real-time observation of transient electron density in water irradiated with tailored femtosecond laser pulses," *New J. Phys.* **14**, 75021 (2012).
- A. Vogel, J. Noack, G. Hüttman, and G. Paltauf, "Mechanism of femtosecond laser nanosurgery of cells and tissues," *Appl. Phys. B* **81**, 1015–1047 (2005).
- A. Kaiser, B. Rethfeld, M. Vicanek, and G. Simon, "Microscopic processes in dielectrics under irradiation by subpicosecond laser pulses," *Phys. Rev. B* **61**, 11437–11450 (2000).
- B. K. Ridley, *Quantum Processes in Semiconductors* (Clarendon Press Oxford, 1999).
- A. Q. Wu, I. H. Chowdhury, and X. F. Xu, "Femtosecond laser absorption in fused silica: Numerical and experimental investigation," *Phys. Rev. B* **72**, 085128–085128-7 (2005).
- S. Höhm, A. Rosenfeld, J. Krüger, and J. Bonse, "Femtosecond diffraction dynamics of laser-induced periodic surface structures on fused silica," *Appl. Phys. Lett.* **102**, 054102–054102-4 (2013).
- S. Richter, M. Heinrich, S. Döring, A. Tünnermann, and S. Nolte, "Nanogratings in fused silica: Formation, control, and applications," *J. Laser Appl.* **24**, 042008–1–042008-8 (2012).
- X. L. Liu, X. Lu, X. Liu, T. T. Xi, F. Liu, J. L. Ma, and J. Zhang, "Tightly focused femtosecond laser pulse in air: from filamentation to breakdown," *Opt. Express* **18**, 26007–26017 (2010).
- L. Jiang, and H.-L. Tsai, "A plasma model combined with an improved two-temperature equation for ultrafast laser ablation of dielectrics," *J. Appl. Phys.* **104**, 93101 (2008).
- P. Balling, and J. Schou, "Femtosecond-laser ablation dynamics of dielectrics: basics and applications for thin films," *Rep. Prog. Phys.* **76**, 36502 (2013).
- L. Haahr-Lillevang, K. Wædegaard, D. B. Sandkamm, A. Mouskeftaras, S. Guizard, and P. Balling, "Short-pulse laser excitation of quartz: Experiments and modelling of transient optical properties and ablation," *Appl. Phys. A* **120**, 1221–1227 (2015).
- J. Siegel, and J. Solis, "Imaging of Plasma Dynamics for Controlled Micromachining," *Femtosecond Laser Micromachining: Photonic and Microfluidic Devices in Transparent Materials* **123**, 19–41 (2012).
- E. G. Gamaly, L. Rapp, V. Roppo, S. Juodkazis, and A. V. Rode, "Generation of high energy density by fs-laser-induced confined microexplosion," *New J. Phys.* **15**, 025018–025018-18 (2013).
- L. V. Keldysh, "Ionization in the field of a strong electromagnetic wave," *J. Exp. Theor. Phys.* **20**, 1307 (1965).
- I. H. Malitson, "Interspecimen Comparison of the Refractive Index of Fused Silica," *J. Opt. Soc. Am.* **55**, 1205–1209 (1965).
- L. Sudrie, A. Couairon, M. Franco, B. Lamouroux, B. Prade, S. Tzortzakis, and A. Mysyrowicz, "Femtosecond Laser-Induced Damage and Filamentary Propagation in Fused Silica," *Phys. Rev. Lett.* **89**, 186601–186601-4 (2002).
- S. Zafar, K. A. Conrad, Q. Liu, E. A. Irene, G. Hames, R. Kuehn, and J. J. Wortman, "Thickness and Effective Electron Mass Measurements for Thin Silicon Dioxide Films Using Tunneling Current Oscillations," *Appl. Phys. Lett.* **67**, 1031–1033 (1995).
- N. M. Bulgakova, R. Stoian, and A. Rosenfeld, "Laser-induced modification of transparent crystals and glasses," *Quantum Electron.* **40**, 966–985 (2010).
- P. Martin, S. Guizard, P. Daguzan, G. Petite, P. D'Oliveira, P. Meynadier, and M. Perdix, "Subpicosecond study of carrier trapping dynamics in wide-band-gap crystals," *Phys. Rev. B* **55**, 5799–5810 (1997).
- A. Couairon, and L. Bergé, "Modeling the filamentation of ultra-short pulses in ionizing media," *Phys. Plasmas* **7**, 193 (2000).
- A. Couairon, and A. Mysyrowicz, "Femtosecond filamentation in transparent media," *Phys. Rep.* **441**, 47–189 (2007).
- S. Couris, M. Renard, O. Faucher, B. Lavorel, R. Chaux, E. Koudoumas, and X. Michaut, "An experimental investigation of the nonlinear refractive index (n_2) of carbon disulfide and toluene by spectral shearing interferometry and z-scan techniques," *Chem. Phys. Lett.* **369**, 318–324 (2003).
- A. J. Taylor, G. Rodriguez, and T. S. Clement, "Determination of n_2 by direct measurement of the optical phase," *Opt. Lett.* **21**, 1812 (1996).